Available online at www.sciencedirect.com
ScienceDirect
ELSEVIER
Ultramicroscopy 108 (2008) 481–487
ultramicroscopy
www.elsevier.com/locate/ultramic

# Influence of the overlap parameter on the convergence of the ptychographical iterative engine

Oliver Bunk[a,*], Martin Dierolf[a,b], Søren Kynde[a], Ian Johnson[a], Othmar Marti[b], Franz Pfeiffer[a]

[a]*Swiss Light Source, Paul Scherrer Institut, 5232 Villigen PSI, Switzerland*
[b]*Institute for Experimental Physics, Ulm University, 89069 Ulm, Germany*

Received 5 April 2007; received in revised form 19 July 2007; accepted 1 August 2007

**Abstract**

The ptychographical iterative engine (PIE) algorithm is examined with both simulated and experimental scanning coherent-diffraction microscopy data. The optimum overlap in terms of image quality, dose on the sample and time of measurements is determined using simulated diffraction data. The validity of the results is supported by experimental helium–neon laser light diffraction data.


*PACS:* 42.30.Rx; 42.30.Va; 42.30.−d; 42.30.Kq

*Keywords:* Phase retrieval; Ptychography; Diffractive imaging; Lensless imaging

## 1. Introduction

The scanning coherent-diffraction microscopy technique coined ptychographical iterative engine (PIE) has the potential for overcoming several problems of conventional coherent-diffraction microscopy, namely the limited field of view, twin image and in general non-unique solutions and slow and non-reliable convergence of the iterative data analysis algorithm. This has been demonstrated experimentally for visible wavelengths at 632.8 nm [1] and in the hard X-ray regime at 1.55 Å [2]. The sensitivity of the PIE technique to experimental uncertainties like illumination functions, noise, and errors in the positioning of the sample with respect to the incident beam has been investigated thoroughly in simulations [3]. Here we particularly focus on numerical and experimental investigations of the overlap parameter to obtain the best image quality.

With diffraction-based imaging, a resolution beyond the Rayleigh or Abbe limit for optical elements can be achieved. A fundamental drawback is the phase problem: the recorded real-valued data contain only amplitude information and the equally important knowledge of the phase values is lost. For the different fields of diffraction and microscopy various solutions have been suggested to retrieve the phase information. Ptychography was initially proposed by Hoppe and Hegerl for transmission electron diffraction microscopy [4,5]. In his pioneering work Hoppe describes how finite, coherent illumination can be used to get intensity from interference between Bragg peaks of a crystal and that thereby the phase information can be restored [5]. He shows that recording diffraction patterns at two positions removes the remaining ambiguity between the correct solution and its complex conjugate. The extension to non-periodic objects, for example with phase-shifting plates, and scanning transmission electron-diffraction microscopy in 2D and 3D have been considered by Hoppe as well [6]. Despite some promising proof-of-principle studies with ptychography for crystalline material [7] and with the related Wigner-distribution deconvolution technique that is suited for non-periodic objects [8,9] a real breakthrough has not been achieved so far. The obstacles for these techniques may be seen in complications both on the experimental and data analysis side.

*Corresponding author. Tel.: +41 56 310 3077.
*E-mail address:* oliver.bunk@psi.ch (O. Bunk).

0304-3991/$ - see front matter © 2007 Elsevier B.V. All rights reserved.
doi:10.1016/j.ultramic.2007.08.003

Another branch of phase retrieval became feasible and thereby conceivable with the advent of modern computers and the fast Fourier transform algorithm [10]: iterative algorithms alternating between direct and Fourier space [11,12]. These algorithms have proven to be useful for fields like astronomy, lensless imaging and digital signal processing. Especially in the field of diffraction-based X-ray imaging impressive results have been reported meanwhile, like for example the imaging of a freeze-dried yeast cell [13,14], lead nanocrystals [15] and a pyramid-like test object [16], as well as the reconstruction of the complex field at the focus of a Fresnel zone plate [17]. Despite these promising results there are some principal limitations. To retrieve a unique set of phases oversampling of the diffraction data is needed which means that a known support for the object under investigation is required [11,12]. Therefore a standard procedure in microscopy—getting a low resolution overview of a comparably large area and then zooming into a region of interest—is not feasible. Additionally, sample preparation is rather cumbersome. Even with oversampled diffraction data iterative phase retrieval has the problem that both the true solution and its complex-conjugate twin image are valid solutions. This can, in practice, be a rather important restriction since the iterative phase retrieval algorithm may stagnate with superpositions of these two solutions. Furthermore, there is an ambiguity of the focal plane, at least in two dimensions. Even if a remedy for all these problems is found, the convergence of the iterative phase retrieval algorithms is rather slow, with typically thousands of iterations, and upon moving towards 3D tomography considerable computing resources are needed [16].

Only recently, more than 30 years after the advent of ptychography and iterative phase retrieval, Faulkner and Rodenburg suggested combining both methods to the so-called ptychographical iterative engine (PIE), using the redundant information of overlapping illuminations at different positions of probe with respect to sample [18,19]. The technique resolves the twin-image problem and the focal plane ambiguity. It yields the complex-valued field in the focal plane and converges fast. First experimental laser light [1] and X-ray [2] results indicate that this technique potentially provides a breakthrough for high-resolution imaging in all cases where coherent radiation is available and multiple exposures of an unaltered sample are possible.

In view of the high potential of this technique it is worthwhile investigating the optimum conditions for conducting PIE experiments. Following up the thorough simulations of Faulkner and Rodenburg [3], investigating the error tolerance of the algorithm, we present here numerical and experimental results on the optimum overlap between the different illuminations taking both image quality and dose on the sample into account. We demonstrate the validity of the results with experimental data recorded with visible laser light.

## 2. PIE algorithm

The details of the algorithm can be found elsewhere [18,19]. To provide a basis for the following we briefly summarize it here. Prerequisite for PIE is a well-known, substantially localized and mainly coherent illumination, for example with electrons, X-rays or visible laser light. This probe described by the complex-valued probe function $P(\mathbf{r})$ is incident on the complex-valued object $O(\mathbf{r})$. The resulting exit wave $\Psi(\mathbf{r}) = P(\mathbf{r})O(\mathbf{r})$ evolves in the far-field to a complex-valued diffraction pattern. The recorded real-valued far-field intensities $I(\mathbf{q})$ are proportional to the absolute square of the Fourier transform of the exit field: $I(\mathbf{q}) \propto |\mathcal{F}[\Psi(\mathbf{r})]|^2$. The momentum transfer $\mathbf{q}$ is the reciprocal coordinate to the direct space coordinate $\mathbf{r}$. It can, for example, be calculated using Bragg's law, $q = 2k\sin(\Theta)$, with the wave number $k = 2\pi/\lambda$ calculated from the wavelength $\lambda$ of the incident illumination and the angle $2\Theta$ between the propagation direction of the incident probe and the scattered part in the direction of $\mathbf{q}$. The far-field intensities are recorded for different sample-to-probe positions shifted by a vector $\mathbf{R}_i$ with respect to the arbitrarily chosen origin. The illuminated positions must overlap, as is detailed in Section 3. The setup for recording such diffraction data can be as simple as the one shown in Fig. 1. It is rather generic and can, for example, be used with X-rays as well [2]. Details of the laser-light PIE setup are described in Section 4.1.

The first iteration $n = 1$ of the phase retrieval is started with, e.g., a random guess for the object function $O(\mathbf{r})$.

(1) The exit field is calculated from the known illumination and the current guess of the object:

$$\Psi_{n,i}(\mathbf{r}) = P(\mathbf{r})O_n(\mathbf{r} + \mathbf{R}_i). \quad (1)$$

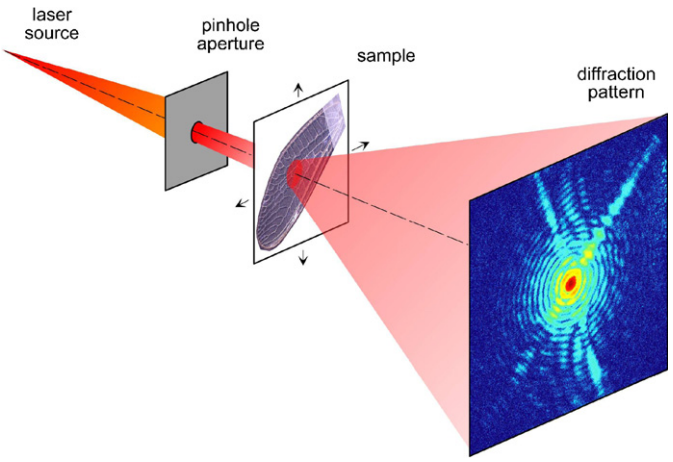


Fig. 1. Laser PIE setup. The pinhole defines the coherent portion of the incident beam that is used for the experiment. The object can be moved in the plane perpendicular to the propagation direction of the incident beam. The diffraction image is recorded with a CCD detector.

(2) Amplitude and phase in reciprocal space are calculated from the Fourier transform of the exit field:

$$A_{n,i}(\mathbf{q})\exp(\mathrm{i}\phi_{n,i}(\mathbf{q})) = \mathscr{F}[\Psi_{n,i}(\mathbf{r})].$$

(3) The amplitudes are set to the measured values:

$$A_{n,i,\mathrm{meas.}}(\mathbf{q}) = \sqrt{I_i(\mathbf{q})}.$$

(4) An updated guess for the exit field is obtained by inverse Fourier transform:

$$\Psi_{n,i,\mathrm{new}}(\mathbf{r}) = \mathscr{F}^{-1}[A_{n,i,\mathrm{meas.}}(\mathbf{q})\exp(\mathrm{i}\phi_{n,i}(\mathbf{q}))].$$

(5) The guess of the object is updated at the position of the current illumination:

$$O_{n+1}(\mathbf{r}+\mathbf{R}_i) = O_n(\mathbf{r}+\mathbf{R}_i) + \beta U(\mathbf{r})(\Psi_{n,i,\mathrm{new}}(\mathbf{r}) - \Psi_{n,i}(\mathbf{r})), \quad (2)$$

with the update function

$$U(\mathbf{r}) \equiv \frac{|P(\mathbf{r})|}{\max(|P(\mathbf{r})|)}\frac{P^*(\mathbf{r})}{|P(\mathbf{r})|^2+\alpha}.$$

(6) These steps are repeated for each position, $i$, and for as many iterations, $n$, as wanted. The deviation between measured and calculated intensities may be monitored via a normalized sum of the squared deviations $S$ or a similar measure [20]:

$$S = \frac{\sum(I_i - A_{n,i}^2)^2}{\sum I_i^2}. \quad (3)$$

The summation is over both the positions, $i$, and the values in the intensity matrix at each position.

The parameter $\beta$ in Eq. (2) is a feedback parameter with $|\beta| \leqslant 1$, typically $\beta \in [0.9, 1.0]$. The parameter $\alpha$ in the update function $U$ prevents numerical instabilities for $|P(\mathbf{r})| \approx 0$. The absolute value is not critical. For example, $\alpha = 0.001$ is suitable for a probe function normalized to 1. The part $|P(\mathbf{r})|/\max(|P(\mathbf{r})|)$ of the update function ensures that the object is mainly changed at positions where the probe has its highest magnitude. The part $P^*(\mathbf{r})/|P(\mathbf{r})|^2$ removes the initial multiplication with the probe function in Eq. (1) from the exit wave, i.e., yields the object function.

## 3. Simulations

An error metric that describes deviations between measured and calculated intensities, like the one in Eq. (3), is not sufficient for judging the quality of a retrieved complex-valued image or the algorithm used for this retrieval. There may be solutions which reproduce the measured intensities in reciprocal space equally well whereas they are not equally close to the true solution for the unknown phase. This motivates us to rely on simulations for the numerical evaluation of the retrieved phases and thereby of the algorithm. In simulations the true solution is known and it is straightforward to define an error metric that describes the deviations from this solution, taking into account both amplitude and phase.

With the term 'overlap' a linear distance offset is meant, not area overlap. For two circles of radius $r$ and the center-to-center distance $a \in [0, 2r]$ we define the absolute overlap $o_{\mathrm{abs}}$ as $o_{\mathrm{abs}} = 2r - a$. Normalized by the diameter of the circles the relative overlap $o$ is given by

$$o = 1 - \frac{a}{2r}. \quad (4)$$

In this article we only consider square grids of illumination positions. The technical advantage of specifying an overlap in distance rather than area is that this typically is directly the parameter that is specified for a scan over several object positions. The specifications of 'relative overlap' in the following neglect the change of the incident illumination by free-space propagation from the defining aperture to the object, i.e., the normalization is done directly by the diameter of the pinhole.

### 3.1. Error metric

The error metric should quantify deviations of the retrieved complex-valued object $O_n$ in iteration $n$ from the known, true solution $O$. An overall phase offset $\exp(\mathrm{i}\gamma)$ to $O_n$ ($\gamma \in \mathbb{R}$) should not change the value of the error metric. The occurrence of such a phase offset is inherent to both conventional iterative phase retrieval and PIE. For the simulations presented here we use an error metric described by Fienup [21]:

$$E \equiv \left(\frac{\sum|O_n|^2 + \sum|O|^2 - 2|\sum OO_n^*|}{\sum|O|^2}\right)^{1/2}. \quad (5)$$

### 3.2. Simulated diffraction data

For the simulations a fluorescence image of a cell was used [22], see Fig. 2. The illumination was defined by a circular aperture of 200 μm (40 pixels) diameter in $z = 2.5$ mm distance from the object. The probe at the sample position $P_z$ can be calculated from the probe at the pinhole position $P_0$ by multiplication with the Fresnel propagator in Fourier space:

$$P_z = \mathscr{F}^{-1}[\exp(-\mathrm{i}zq^2/(2k))\mathscr{F}[P_0]],$$

with $k = 2\pi/(632.8\,\mathrm{nm})$. The object had $201 \times 201$ pixel of $5\,\mu\mathrm{m} \times 5\,\mu\mathrm{m}$ each. The detector was in the far-field, i.e., linked to the illuminated object by a discrete Fourier transform. The sample image and four diffraction patterns are shown in Fig. 2.

### 3.3. Simulation results

To determine the optimum overlap of the different illumination positions the object shown in Fig. 2(a) was

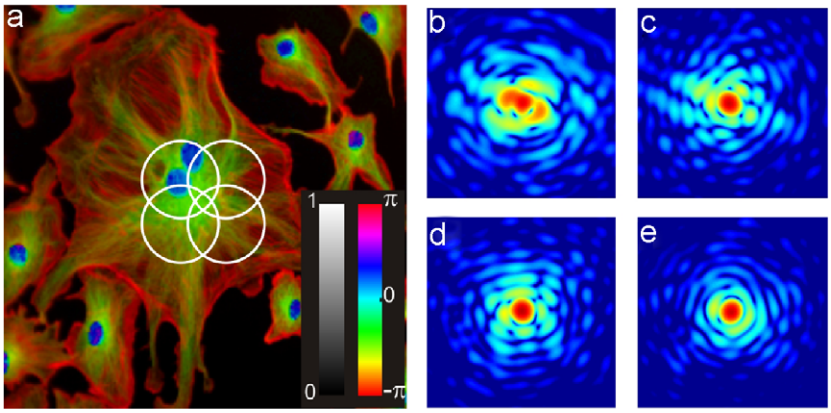


Fig. 2. Sample image and some diffraction patterns. (a) Image used for the simulations. Representing the colors of this image in the hue, saturation and value color space the hue was taken as phase and the amplitude as value (i.e., brightness). The saturation was set to 100%. (b)–(e) Diffraction patterns for the positions indicated in the image. The amplitude, i.e., the square-root of the intensity, is plotted on a color-coded logarithmic scale.

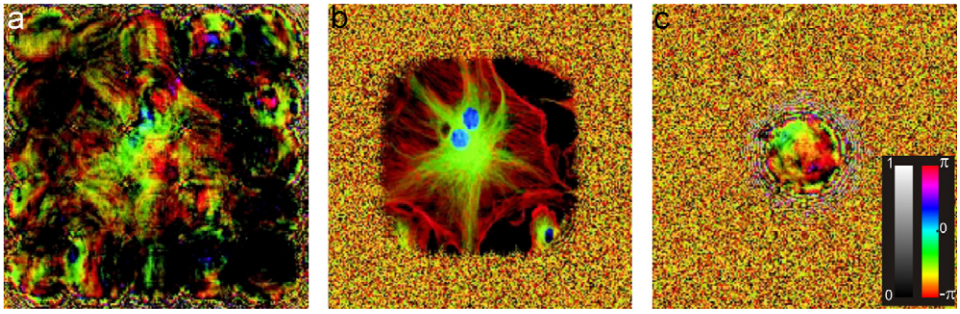


Fig. 3. Reconstructions of simulated data for different relative overlaps. The test object is shown in Fig. 2. Each image has been retrieved in 30 PIE iterations over $5 \times 5$ object positions. The relative overlap of the object positions was 10% (a), 60% (b), and 100% (c).

scanned with $5 \times 5$ positions of different overlaps. The result is shown in Fig. 3. In Fig. 3(a) the relative overlap of the positions, see Eq. (4) for a definition, is only 10%. In 30 PIE iterations the similarity to the original image is barely visible, however, still much better than with iterative phase retrieval that does not make use of the overlap information, after the same number of iterations. When the relative overlap is increased to 60%, the retrieved image cannot be distinguished by eye from the original one, see Fig. 3(b). With 100% relative overlap the PIE algorithm degenerates to a conventional iterative phase retrieval using the hybrid input–output algorithm. The image quality is again poor, especially if one takes into account that 30 iterations over 25 fully overlapping positions actually correspond to 750 iterations at the central position. However, for a direct comparison one has to take into account, that the support constraint for the hybrid input–output algorithm is a known illumination function rather than the usual known object region.

To quantify these results the error metric $E$, defined in Eq. (5) as a measure for the quality of the retrieved image, was monitored as a function of the overlap of neighboring positions. The error was calculated for the central of the $5 \times 5$ object positions to avoid any edge effects and to neglect unilluminated areas. To provide a statistical basis each PIE run was repeated 25 times, starting each time from another random guess. The average error and its standard deviation are shown in Fig. 4(a) as a function of the relative overlap and for different numbers of PIE iterations. There are two important results: (i) The optimum image quality is obtained for a very high overlap of about 85%. One should refrain from using higher overlaps since the gradual transition to the standard hybrid input–output algorithm in the range from about 85% to 100% leads to a rapid increase of the error $E$. (ii) With sufficient relative overlap of at least 50% and as little as five PIE iterations, the image quality is already good, probably sufficiently good for a fast on-line feedback. Continuing to only 30 iterations the image quality is excellent. Nevertheless, a minor improvement of the image quality is still measurable for more iterations.

By visual inspection of Fig. 3(b) it becomes clear, that an error of below $10^{-2}$ for 60% relative overlap is already an excellent value. For practical purposes therefore the question arises, what the optimum overlap is, taking the total time of measurements and the radiation dose on the sample into account. The optimum overlap will clearly not any longer be about 85%, but its precise value will depend on various factors like the weight given to acquisition time relative to image quality, whether the

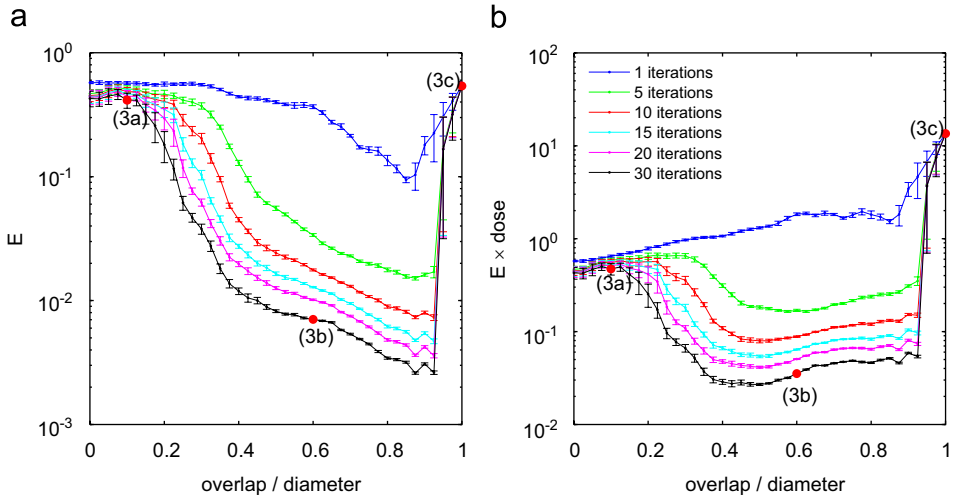


Fig. 4. Error as a function of the relative overlap of the illuminated areas and for different numbers of iterations. In (a) the error $E$ as a measure for the image quality is plotted. In (b) the dose on the sample is linearly taken into account by plotting $E$ times the dose. The error bars specify the standard deviation when averaging the results of 25 simulation runs. The red dots mark the parameters for the images in Fig. 3.

radiation damage increases continuously or starts at a certain minimum dose and the form of the progression of the radiation damage. These factors depend very much on the individual experiment.

We calculate the dose as the illumination hitting a pixel of the object. With the incident probe $P$ being normalized to 1, e.g., a dose of 2.0 means that the corresponding pixel has been fully illuminated twice. As a guide-line the dose is taken linearly into account by plotting the error multiplied by the dose in Fig. 4(b). This gives an optimum relative overlap of less than 60%. The same result would be obtained if the scanning time overhead is quantified via unnecessary over-exposures. If the broadening of the incident illumination due to free-space propagation is not taken into account then the minimum relative overlap for complete coverage of the object is $1-2^{-1/2} \approx 29\%$. The error of the retrieved image at this overlap is higher than under optimal conditions but sufficiently low if radiation damage and speed are a major concern.

We verified these results with other test objects and obtained qualitatively the same error plots indicating that these simulations have some general validity. It should be noted that it is sufficient to have overlapping illuminations along one dimension, i.e., each illumination is only constrained by up to two neighboring illuminations. The convergence of the PIE algorithm is improved by having overlapping illuminations in more dimensions but due to the two-dimensionality of each illumination is the algorithm sufficiently constrained by one-dimensional overlap. This may be interesting for certain applications like scanning rod-like objects or quick overview scans in on-line imaging.

To summarize the results of the simulations: emphasizing image quality without neglecting completely the dose on the sample and the time needed for the measurements, a relative overlap of 60% of the diameter of the defining pinhole seems to be adequate. Even if radiation dose is not an issue, the overlap should not exceed 85% for an optimum performance of the algorithm. For fast overview scans and very radiation sensitive objects, like any biological sample, relative overlaps of only 30% seem to be advisable.

## 4. Measurements

The results of the simulations have been verified experimentally using a laser setup. Using visible laser light has the advantage that the influence of several potential sources of experimental uncertainties can be reduced considerably. For instance, compared to X-ray experiments [2], in laser experiments the influence of vibrations and uncertainties in the precise object position are reduced due to the larger diameter of the incident illumination and the longer wavelength. Furthermore, the source is fully coherent, i.e., partial coherence is not an additional source of errors.

### 4.1. Experimental setup

The experimental setup is schematically depicted in Fig. 1. A HeNe laser, $\lambda = 632.8$ nm, was used (Melles Griot 25 LHP 151-230, 5 mW, $TEM_{00}$). The incident beam was defined by a 200 μm pinhole in 1.5 mm distance from the sample. The sample was motorized in all three directions using stepper motor driven linear translation stages with a half-step size of approximately 0.24 μm (Newport MFA-PP). To reduce the influence of stray light and to adjust the incident intensity to the very sensitive detector a combination of a narrow laser-line bandpass filter and three absorptive neutral density filters has been used (Edmund Optics). A charge coupled device (CCD, IMG 1001E, Finger Lakes Instrumentation) was placed at a distance of 200 mm from the sample. The CCD chip has 1024 × 1024 pixels of 24 μm × 24 μm size and 16 bit dynamic range. It is

Peltier cooled to −25 °C to reduce the dark noise of the chip. The filters are connected to the CCD by a light-tight tube composed of C-mount and T-mount elements (Edmund Optics) to prevent any light from entering the detection system from the side. To ease alignment of the setup it was placed on rails (FLS 95, Linos) mounted on an optical table and the laser source, pinhole and detector could manually be adjusted with suitable tilt and translation units (Ekspla). The sample positioning and the detector were controlled with the program spec (Certified Scientific Software).

As for any lensless diffraction experiment, the high dynamic range and low noise of the detector are of utmost importance since they determine directly the accessible range in momentum transfer and thereby the resolution. To increase the dynamic range multiple exposures may be used. Especially useful are exposure series of different exposure lengths, deliberately overexposing the central part of the diffraction pattern. However, this is only feasible if the detector does not have too significantly a 'blooming', i.e., spill-over from overexposed regions and if the detector is not damaged by the overexposure. For the data

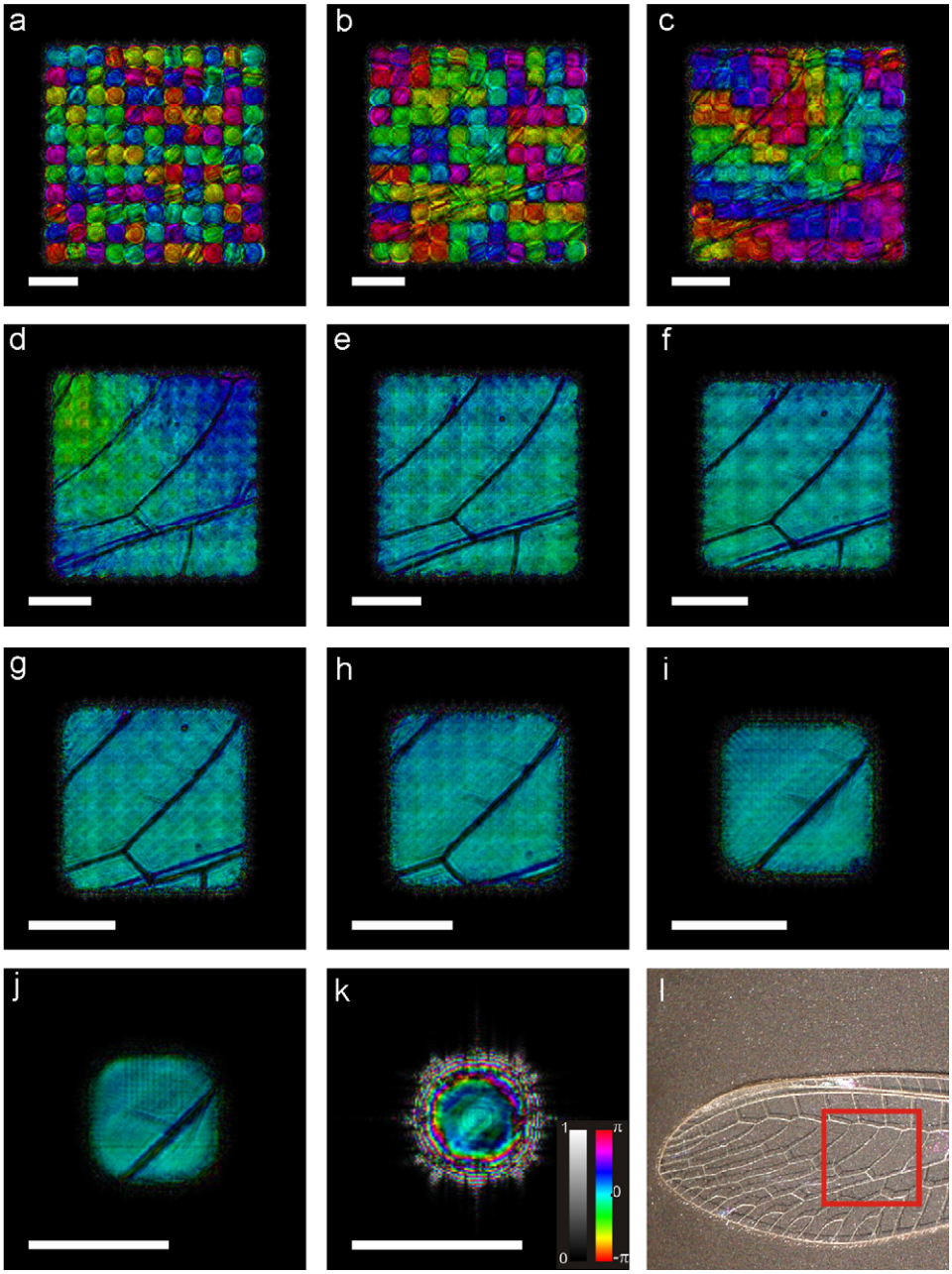


Fig. 5. Amplitude and phase images retrieved from measured data sets for different relative overlaps. The relative overlap is increased in steps of 10% from 0% (a) to 100% (k). The white scale-bar represents 0.5 mm. In (l) a light-microscope image of the sample is shown. The red frame marks the region covered in (a). Brightness represents amplitude and hue codes phase according to the colorbar in K.

presented here single exposures are used, exploiting almost the full dynamic range of the CCD.

### 4.2. Experimental results

As test sample a fly wing was used. A light microscope image of the sample is shown in Fig. 5(1). The sample was scanned with $11 \times 11$ positions with relative overlaps ranging from 0% to 100%. The retrieved complex-valued object is represented as a HSV false color plot in Fig. 5(a)–(k), again representing the phase by the hue and the amplitude by the brightness (i.e., the value). The reconstructed images are retrieved with an arbitrary phase offset. This is an inherent feature of such iterative phase retrieval procedures, as discussed before. To ease comparison, this phase offset has been adjusted for the images in Fig. 5(a)–(k).

In Fig. 5(a) one sees that for nominally 0% overlap the average phase of individual positions is slightly correlated. That some neighboring positions have similar average phase and that some amplitude features are visible at all is caused by the overlap of the weak tails of the incident probe due to free-space propagation from the pinhole to the object. With increasing overlap the individual phase values become more and more correlated as evident by the larger patches of similar color in Fig. 5(c). The retrieved image for the recommended minimum overlap of 30% is shown in Fig. 5(d). There are no not illuminated patches within the scanned area and the image quality is good. At the recommended optimum overlap value of 60%, Fig. 5(g), the highly absorbing lines are well defined and artifacts in the background are further reduced. Up to 90% overlap, Fig. 5(j), the quality of the image is only little improved at the expense of a considerable overhead in terms of scanning time and dose on the sample. The standard iterative phase retrieval with known-illumination constraint to which the PIE algorithms becomes at 100% overlap, Fig. 5(k), retrieves a low quality image of the central part of the scanned area within the 30 PIE iterations over $11 \times 11$ positions, i.e., within a total of 3630 iterations for a rather small area.

In summary, the experimental data confirm the results of the simulations concerning the optimum overlap.

## 5. Summary and conclusion

The optimum overlap of different illuminations has been examined for the PIE algorithm with both simulated and experimental scanning coherent diffraction-microscopy data. The quality of the retrieved images has been considered as well as the time for the measurements and the dose on the sample. A relative overlap of 60% yields high quality complex-valued reconstructions of the scanned object area. An overlap of only 30% may be advisable if low dose and high speed receive higher priority.

## Acknowledgments

This work was performed at the Swiss Light Source, Paul Scherrer Institut, Villigen, Switzerland. We thank Harun H. Solak for providing the HeNe laser, Xavier Donath for technical assistance and Andreas Menzel, John M. Rodenburg, Andrew C. Hurst, and Anthony C. Cullis for fruitful discussions.

## References

[1] J.M. Rodenburg, A.C. Hurst, A.G. Cullis, Ultramicroscopy 107 (2007) 227.
[2] J.M. Rodenburg, A.C. Hurst, A.G. Cullis, B.R. Dobson, F. Pfeiffer, O. Bunk, C. David, K. Jefimovs, I. Johnson, Phys. Rev. Lett. 98 (2007) 034801.
[3] H.M.L. Faulkner, J.M. Rodenburg, Ultramicroscopy 103 (2005) 153.
[4] R. Hegerl, W. Hoppe, Ber. Bunsen-Ges. 74 (1970) 1148.
[5] W. Hoppe, Acta Cryst. A 25 (1969) 495.
[6] W. Hoppe, Acta Cryst. A 25 (1969) 508.
[7] P.D. Nellist, B.C. McCallum, J.M. Rodenburg, Nature 374 (1995) 630.
[8] J.M. Rodenburg, R.H.T. Bates, Philos. Trans. R. Soc. London A 339 (1992) 521.
[9] H.N. Chapman, Ultramicroscopy 66 (1996) 153.
[10] J.W. Cooley, W. Tukey, Math. Comput. 19 (1965) 297.
[11] R.W. Gerchberg, W.O. Saxton, Optik 35 (1972) 237.
[12] J.R. Fienup, Appl. Opt. 21 (1982) 2758.
[13] D. Shapiro, P. Thibault, T. Beetz, V. Elser, M. Howells, C. Jacobsen, J. Kirz, E. Lima, H. Miao, A.M. Neiman, D. Sayre, Proc. Natl. Acad. Sci. USA 102 (2005) 15343.
[14] P. Thibault, V. Elser, C. Jacobsen, D. Shapiro, D. Sayre, Acta Cryst. A 62 (2006) 248.
[15] M.A. Pfeifer, G.J. Williams, I.A. Vartanyants, R. Harder, I.K. Robinson, Nature 442 (2006) 63.
[16] H.N. Chapman, A. Barty, S. Marchesini, A. Noy, S.P. Hau-Riege, C. Cui, M.R. Howells, R. Rosen, H. He, J.C.H. Spence, U. Weierstall, T. Beetz, C. Jacobsen, D. Shapiro, J. Opt. Soc. Am. A 23 (2006) 1179.
[17] H.M. Quiney, A.G. Peele, Z. Cai, D. Paterson, K.A. Nugent, Nature Phys. 2 (2006) 101.
[18] J.M. Rodenburg, H.M.L. Faulkner, Appl. Phys. Lett. 85 (2004) 4795.
[19] H.M.L. Faulkner, J.M. Rodenburg, Phys. Rev. Lett. 93 (2004) 023903.
[20] E.H. Linfoot, Fourier Methods in Optical Image Evaluation, Focal Press, London, 1964.
[21] J. Fienup, Appl. Opt. 36 (1997) 8352.
[22] Invitrogen Corporation, ⟨http://www.invitrogen.com⟩.